Role of spin-phonon and electron-phonon interactions in the phonon renormalization of $(Eu_{1-x}Bi_x)_2Ir_2O_7$ across the metal-insulator phase transition: Temperature-dependent Raman and x-ray studies

Anoop Thomas,[1] Prachi Telang,[2] Kshiti Mishra ⓘ,[2] Martin Cesnek,[3] Jozef Bednarcik ⓘ,[4,*] D. V. S. Muthu ⓘ,[1] Surjeet Singh,[2] and A. K. Sood ⓘ[1,†]

[1]*Department of Physics, Indian Institute of Science, Bangalore 560012, India*

[2]*Department of Physics, Indian Institute of Science Education and Research, Dr Homi Bhabha Road, Pune 411008, India*

[3]*Department of Nuclear Reactors, Faculty of Nuclear Sciences and Physical Engineering, Czech Technical University in Prague, V Holesovickach 2, 180 00 Prague, Czech Republic*

[4]*Deutsches Elektronen-Synchrotron DESY, Notkestrasse 85, D-22607 Hamburg, Germany*

We report temperature-dependent Raman scattering and x-ray diffraction studies of pyrochlore iridates $(Eu_{1-x}Bi_x)_2Ir_2O_7$, for $x = 0$, 0.02, 0.035, 0.05, and 0.1. The temperature variation in Raman experiments spans from 4 to 300 K, covering the metal-insulator phase transition accompanied by paramagnetic–to–all-in/all-out (AIAO) spin ordering (T_N). These systems also show a Weyl semimetal (WSM) phase at low temperatures ($< \sim 50$ K). The Ir-O-Ir bond bending mode A_{1g} (510 cm^{-1}) shows anomalous softening (for $x = 0.0$, 0.02, 0.035, and 0.05) in the magnetically ordered AIAO state, arising primarily from the spin-phonon interaction due to the phonon modulation of the Dzyaloshinskii-Moriya spin-exchange interaction. The two stretching modes T_{2g}^1 (307 cm^{-1}) and T_{2g}^2 (382 cm^{-1}) harden significantly in the magnetic insulating phase. The T_{2g} phonons (for $x = 0.0$, 0.02, 0.035, and 0.05) also show anomalous temperature dependence of their mode frequencies above T_N due to strong electron-phonon coupling. The signatures of the WSM state are observed clearly in phonon renormalization <50 K (in $x = 0.02$) due to strong electron-phonon interaction. Our experimental results establish strong magneto-elastic coupling below T_N and significant electron-phonon interactions in the metallic phase above T_N as well as in the low-temperature WSM state.

I. INTRODUCTION

There has been an upsurge of interest in understanding exotic properties of pyrochlore iridium oxides ($A_2Ir_2O_7$, A = lanthanide, Bi, Pb, or Y) due to large spin-orbit coupling (SOC) arising from heavy iridium atoms, intermediate electron correlations, and geometry-induced spin frustration [1–4]. Heisenberg antiferromagnetic isotropic exchange (IE) interactions make the iridium (Ir^{4+}) effective spin $\frac{1}{2}$ on a tetrahedral motif frustrated, preventing the spins to have a long-range magnetic ordering. However, the Dzyaloshinskii-Moriya (DM) interactions arising from strong SOC competes with Heisenberg interactions to result in an ordered antiferromagnetic structure with all-in/all-out (AIAO) ground state below the transition temperature T_N in pyrochlores with small ionic radii A such as Lu, Yb, Ho, Y, Dy, Tb, Gd, Eu, Sm, and Nd. At low temperatures, the DM interaction wins over Heisenberg interaction in the iridates having smaller A^{3+} size, resulting in a magnetic insulating phase. The electron hopping arising from the chemical pressure of the A^{3+} site can suppress this magnetic ordering in $Pr_2Ir_2O_7$ and

$Bi_2Ir_2O_7$ at low temperatures [5–7]. On the other hand, the paramagnetic-to-antiferromagnetic phase transition in three iridates $Eu_2Ir_2O_7$, $Sm_2Ir_2O_7$, and $Nd_2Ir_2O_7$ is accompanied by a metal-insulator transition (MIT) without change of crystal symmetry [8–10]. Theoretical calculations show that, below the MIT temperature, topological phases like the Weyl semimetal (WSM), axion insulator, and topological Mott insulator phases are possible [2,3,11]. The experimental probes to show the topological phases in pyrochlore iridates include optical conductivity, resistivity, and angle-resolved photoemission spectroscopy along with varying pressure, temperature, and doping [12–16]. The WSM state at low temperatures has been seen in optical conductivity measurements in $Eu_2Ir_2O_7$ by way of the linear temperature dependence of optical conductivity below the Néel temperature T_N and interband optical conductivity vanishing at low frequencies [12]. The Drude spectral weight was found to be independent of temperature in the metallic phase, whereas it decreased smoothly in the AIAO phase. Simultaneous pressure and temperature-dependent electrical transport experiments have also shown a quantum critical point in $Eu_2Ir_2O_7$ <120 K and >6 GPa [13].

Like physical pressure, quantum criticality is observed with chemical doping also. Doping can be done by substitution of A^{3+}- or Ir^{4+}-site atoms. The substitution of Ir^{4+} with Rh^{4+} and Ru^{4+} reduces SOC strength [17–19], whereas isovalent substitution in A^{3+} atoms results in tuning of the

───────

*Present address: Institute of Physics, Faculty of Science, P.J. Safarik University in Kosice, Park Angelinum 9, 041 54 Kosice, Slovak Republic.

†asood@iisc.ac.in

electronic bandwidth. Since the topological states arise from Ir^{4+} electrons, the study of electronic and magnetic phases is richer when the nonmagnetic A^{3+} ion is substituted. Telang *et al.* [16] have studied emerging electronic and magnetic phases in $Eu_2Ir_2O_7$ with bismuth (Bi) doping. Since the lattice constant of $Bi_2Ir_2O_7$ (10.3307 Å) is higher than $Eu_2Ir_2O_7$ (10.2989 Å), the isovalent substitution of Eu^{3+} with Bi^{3+} should increase the lattice parameter in $(Eu_{1-x}Bi_x)_2Ir_2O_7$ with x as per Vegard's law. In contrast, an anomalous lattice volume decrease is observed in $(Eu_{1-x}Bi_x)_2Ir_2O_7$ for $x = 0.02$ to 0.035. Further, resistivity for these systems at low temperatures follows $1/T^\alpha$, suggesting the phase to be close to the WSM phase [16]. For $x = 0.02$, $\alpha \sim 1$, and combining the transport data with the measurements of the Seebeck coefficient, it has been proposed that the low-temperature phase is WSM, with the Fermi energy close to the Weyl nodes. For $x = 0$, the Fermi energy is below the Weyl nodes (i.e., hole doped), whereas for $x = 0.035$, the Fermi energy is above the Weyl nodes (i.e., electron doped) [16].

In recent years, the role of electron-phonon interaction has been recognized as important in understanding electronic properties and phase behavior of pyrochlore iridates [20]. Another interaction found to play a crucial role in transition metal oxides is the spin-phonon coupling which has led to the observation of phenomena such as the thermal Hall effect [21,22], stabilization of magnetic order with epitaxial strain [23,24], and spintronics [25]. Raman [18,26] and infrared [27] studies on some of the pyrochlore iridates show phonon anomalies at and below T_N. For example, Raman studies on $Eu_2Ir_2O_7$ [26] show an anomalous softening and line shape anomalies of the Ir-O-Ir bending vibration, the E_g mode, below T_N, attributed to the strong coupling of the E_g phonon to spin, charge, and orbital excitations. Notably, they did not see any anomaly in the other Ir-O-Ir bending vibration of the A_{1g} symmetry or in the remaining Raman allowed modes. Recent infrared studies of $Y_2Ir_2O_7$ [27] have brought out that the phonon softening of Ir-O-Ir-bending-related vibrations arises due to spin-phonon coupling mediated by the DM interaction rather than the commonly considered IE interaction. Motivated by these experiments, we have done a detailed temperature-dependent Raman study of $(Eu_{1-x}Bi_x)_2Ir_2O_7$ ($x = 0$, 0.02, 0.035, 0.05, and 0.1) and show that the A_{1g} mode associated with Ir-O-Ir bending vibration and the other two low-frequency T_{2g} modes show phonon anomalies. Further, the T_{2g} modes show anomalous hardening (as temperature increases) above T_N due to electron-phonon interaction. Notably, signatures of the WSM phase are seen <50 K in the temperature dependence of phonon frequencies and linewidths.

II. METHODS

Polycrystals of $(Eu_{1-x}Bi_x)_2Ir_2O_7$ were synthesized by the solid-state reaction route and characterized by high-resolution x-ray synchrotron diffraction, electrical resistivity, thermoelectric power, muon spin resonance, and specific heat, as reported in our recent work [16]. The MIT, accompanied by magnetic order, is observed in samples with $x = 0$, 0.02, 0.035, and 0.05 at temperatures 122, 115, 108, and 63 K, respectively. For $x = 0.1$, temperature-driven MIT is sup-

pressed, showing metallic behavior throughout the entire temperature range. The low-temperature x-ray diffraction experiments between room temperature and 90 K were carried out on a series of compositions $(Eu_{1-x}Bi_x)_2Ir_2O_7$ ($x = 0$, 0.02, 0.05, and 0.1) using high-energy photons ($\lambda = 0.020713$ nm) at the Beamline P02.1 of Petra III, DESY in transmission mode [28]. Low-temperature micro-Raman studies (4 to 300 K) were carried out on sintered pellets of $(Eu_{1-x}Bi_x)_2Ir_2O_7$ ($x = 0$, 0.02, 0.035, 0.05, and 0.1) using a continuous flow helium cryostat (M/s Oxford Instruments, Model Microstat) with temperature controller ITC502. After attaining the set temperature, we waited for 10 min before recording the spectra. Raman spectra were recorded using a Horiba LabRam spectrometer in backscattering geometry, using a $50\times$ objective and laser excitation of 532 nm with laser power of ~ 0.4 mW on the sample. Raman spectra were fitted with Lorentzian functions to extract frequency and linewidth [full width at half maximum (FWHM)] of individual Raman modes except the E_g mode which is fitted with the Fano profile $I_F(\omega) = \frac{A_0(1+\frac{\epsilon}{q})^2}{(1+\epsilon)^2}$, where A_0 is the intensity parameter, $1/q$ is the Fano asymmetry parameter, and $\epsilon = (\omega - \omega_0)/\Gamma$, with ω_0 and 2Γ being the phonon frequency and FWHM, respectively, and the error bars on the values of frequencies and linewidth are obtained from the nonlinear least square fitting of data using the software ORIGIN (see also Appendixes A and B).

III. RESULTS

A. X-ray diffraction as a function of temperature and doping

Figures S1(a) and S1(b) in the Supplemental Material [29] show typical x-ray diffraction patterns along with the Rietveld fitting at 300 and 90 K for $x = 0$ and 0.02. As no new Bragg peak is seen at low temperatures for all values of x, this confirms the absence of structural change with doping and with temperature, particularly below T_N. The temperature dependence of lattice parameters of $(Eu_{1-x}Bi_x)_2Ir_2O_7$ ($x = 0$, 0.02, 0.05, and 0.1) in the temperature range of 295 to 90 K are shown in Fig. 1(a). The solid symbols are the extracted lattice parameter after analyzing the x-ray diffractograms. In Fig. 1(a), the lattice parameters for all the doping ($x = 0$, 0.02, 0.05, and 0.1) vary smoothly with temperature. Figure 1(b) confirms the anomalous lattice parameter contraction for $x = 0.02$ at 90 K, like the reported anomaly at room temperature [16]. The solid lines in Fig. 1(a) are fit to the equation $a(T) = a(0)[1 + \frac{be^{c/T}}{T(e^{c/T}-1)^2}]$ [30], where $a(0)$ is the lattice constant at 0 K, and b and c are fitting parameters.

B. Raman spectra at ambient condition

The pyrochlore $A_2B_2O_6O'$ can be viewed by forming tetrahedra networks A_4O' and octahedra BO_6 with A, B, O, and O', respectively, occupying $16c$, $16d$, $48f$, and $8b$ sites. In the pyrochlore structure, there are only two independent variable parameters: (i) the x coordinate of the $O(48f)$ and (ii) the lattice parameter a. The structure belongs to space group Fd-$3m$, and the irreducible representations of optical phonons at the zone center are $\Gamma_{Optical} = A_{1g} + E_g + 2T_{1g} + 4T_{2g} + 3A_{2u} + 3E_u + 7T_{1u} + 4T_{2u}$ [31]. Among these, A_{1g}, E_g, and T_{2g} are
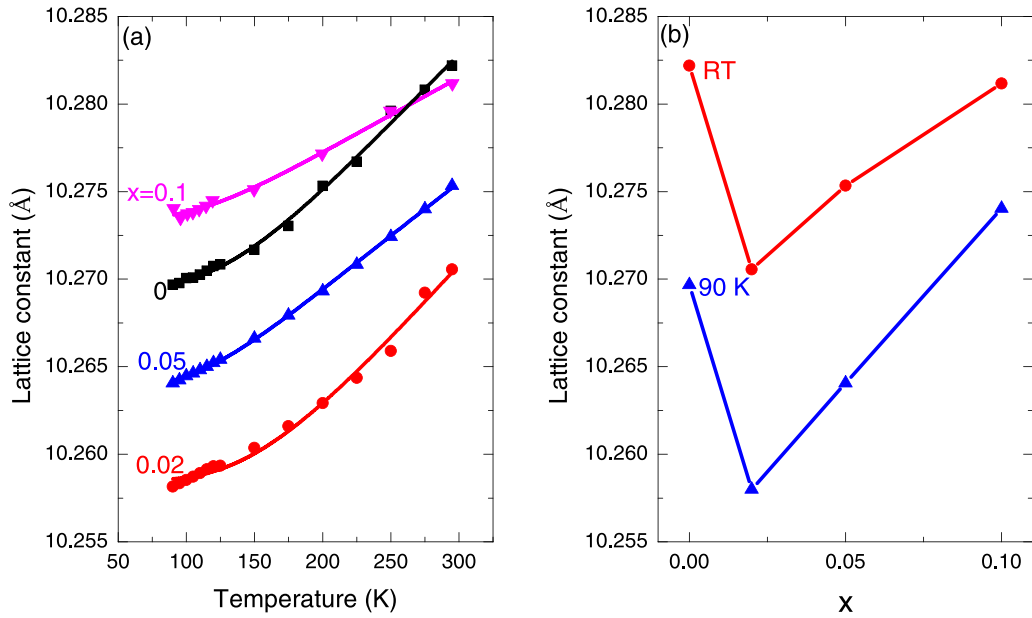
FIG. 1. (a) Variation of the lattice parameter of $(\mathrm{Eu}_{1-x}\mathrm{Bi}_x)_2\mathrm{Ir}_2\mathrm{O}_7$ with temperature. Symbols represent lattice parameters. Solid lines are fit to the data as discussed in the text. (b) Lattice constant vs x at room temperature (RT) and 90 K.

Raman active modes. Because of the inversion symmetry associated with Eu^{+3} and Ir^{+4} sites, heavy cations are stationary in Raman active modes. Six Raman modes at 306.5 (T_{2g}^1), 347 (E_g), 382 (T_{2g}^2), 510.5 (A_{1g}), 541 (T_{2g}^3), and 678.4 (T_{2g}^4) cm^{-1} for undoped $\mathrm{Eu}_2\mathrm{Ir}_2\mathrm{O}_7$ as well as for doped systems are observed (see Appendix A). The seventh mode seen at 703 cm^{-1}, marked as P, is possibly a second-order mode. We could not distinguish clearly T_{2g}^4 and P modes in the doped samples. As mentioned before, the Raman modes in $\mathrm{Eu}_2\mathrm{Ir}_2\mathrm{O}_7$ involve only oxygen atoms in Ir-O, Eu-O, and Eu-O′ stretching and Ir-O-Ir bending vibrations. The stretching of Eu-O bonds dominates the low-frequency T_{2g}^1 and T_{2g}^2 modes in $\mathrm{Eu}_2\mathrm{Ir}_2\mathrm{O}_7$. The T_{2g}^3 mode involves the motion of Eu-O′ stretching, and the high-frequency T_{2g}^4 mode involves predominantly Ir-O stretching. The E_g and A_{1g} modes are associated with the Ir-O-Ir bending [26]. According to Bae *et al.* [32] on $\mathrm{Y}_2\mathrm{Ru}_2\mathrm{O}_7$, the A_{1g} mode changes Ru-O-Ru bond angles in-phase (isotropic), whereas changes are not in-phase for the E_g and T_{2g} modes.

C. Raman studies at low temperatures

Figures 2(a) and 2(b) show Raman spectra for undoped and doped $(\mathrm{Eu}_{1-x}\mathrm{Bi}_x)_2\mathrm{Ir}_2\mathrm{O}_7$ for $x = 0, 0.02, 0.035, 0.05$, and 0.1 at two selected temperatures 300 K (inside cryostat) and 4 K in the spectral range of 150 to 800 cm^{-1}. We observe changes in the spectra recorded at 4 K compared with spectra at 300 K. The undoped $\mathrm{Eu}_2\mathrm{Ir}_2\mathrm{O}_7$ shows a new mode marked $N1$ (strong) at $\sim$211 cm^{-1} (and some weak modes near $N1$ marked as $N2$ to $N5$) appearing below the MIT temperature of 122 K. The $N1$ mode is weak for $x = 0.035$, very broad for $x = 0.05$, and it is absent for $x = 0.1$. The details of the spectral analysis of samples with different x values as a function of temperature are given in Appendix B.

1. Temperature dependence of Raman modes of undoped $\mathbf{Eu_2Ir_2O_7}$

First, we address the phonon anomalies in undoped $\mathrm{Eu}_2\mathrm{Ir}_2\mathrm{O}_7$. Figure 3(a) shows Raman spectra at different temperatures. Figure 3(b) shows the deconvolution of spectra at a few temperatures where the E_g mode is taken to be of Fano line shape and other modes are Lorentzian. Figure 4 shows the temperature dependence of frequency and linewidth of strong modes A_{1g}, T_{2g}^2 and T_{2g}^1, and E_g. As mentioned earlier, the parameters of the E_g mode are the same as in Ref. [26]. A shaded region drawn below $T_N = 122$ K marks the magnetic ordering temperature, clearly showing anomalies and significant changes in this region. To understand the anomalous changes in the frequency and linewidth of the phonons, we first fit the data at temperatures above T_N with the expected changes based on the anharmonic interactions between phonons. In the simplest cubic anharmonic model, a phonon with frequency ω decays into two phonons of equal frequencies $\omega/2$, giving the temperature dependence of frequency and linewidth (Γ) as [33]: $\omega(T) = \omega(0) + CG[\omega(0), T]$ and $\Gamma(T) = \Gamma(0) + DG[\omega(0), T]$, where $G[\omega(0), T] = \{1 + \frac{2}{\exp[\frac{\hbar\omega(0)}{2kT}] - 1}\}$, C and D are phonon-phonon interaction parameters, with $C < 0$ and $D > 0$. We have fitted the observed linewidth and frequency for the T_{2g}^1 and A_{1g} modes with the cubic anharmonic model down to 122 K, shown by solid red lines. The fitted lines are extrapolated to 0 K by the dashed red lines to bring out the anomalous behavior below T_N. For the T_{2g}^2 mode, the anharmonic model with $C < 0$ cannot explain the frequency variation above T_N, and hence, the solid blue line is a guide to the eye.

The following observations are noteworthy: (i) the frequency of the A_{1g} mode shows anomalous temperature dependence: Frequency softens with decreasing temperature below T_N, (ii) the frequencies of T_{2g}^1 and T_{2g}^2 modes increase sharply below T_N, (iii) the linewidths of T_{2g}^1 and T_{2g}^2 modes
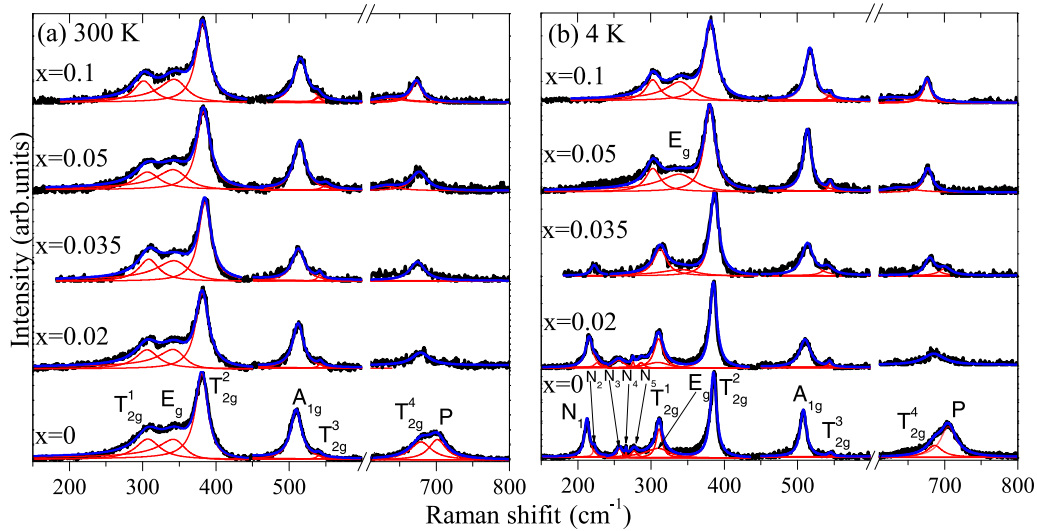
FIG. 2. Raman spectra of $(Eu_{1-x}Bi_x)_2Ir_2O_7$ at (a) 300 K and (b) 4 K for $x = 0$, 0.02, 0.035, 0.05, and 0.1. The thick black line represents raw data that are fitted with sum of individual functions (shown by blue lines) discussed in the text. The red line represents individually fitted Raman modes.

below T_N decrease much more than predicted by the anharmonic model, and (iv) the frequency of the T_{2g}^2 mode increases above T_N, an anomalous trend opposite to the anharmonic and quasiharmonic effects seen for the other two modes. As the E_g mode is shown to redshift with decreasing temperature by ~35 cm^{-1} [26], it gets overlapped with the T_{2g}^1 mode [Figs. 3(b) and 4]. It is seen that the presence of the T_{2g}^1 mode can be deciphered up to 4 K, where its fre-

quency is like that of the E_g mode. This gives confidence in the observed temperature dependence of the T_{2g}^1 mode frequency and linewidth below T_N. The observations (i) to (iii) point to strong spin-phonon coupling in the AIAO phase. The observation (iv), namely, the frequency increase with increasing temperature above T_N, can only arise due to strong electron-phonon interaction of the T_{2g}^2 mode in the metallic phase.
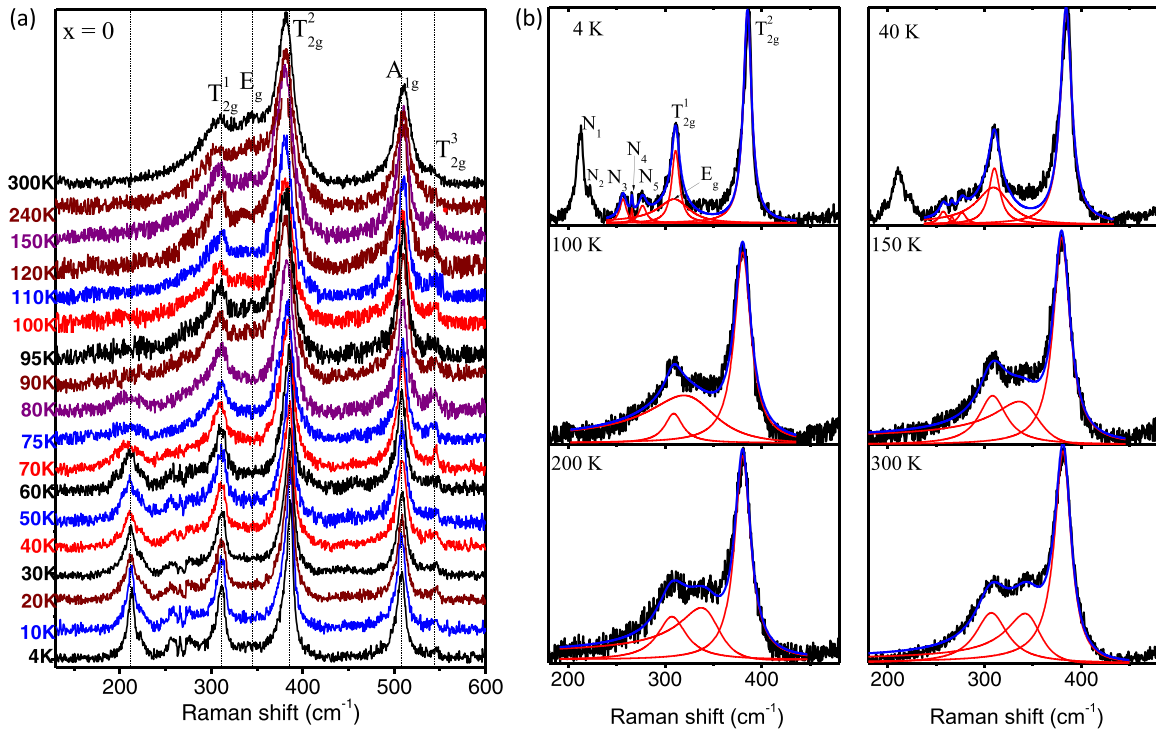
FIG. 3. (a) Raman spectra for the $x = 0$ compound at several temperatures. The dotted lines show the peak position for different modes. (b) The representative plots for fitted data in the range of 180 to 480 cm^{-1}, covering T_{2g}^1, E_g, and T_{2g}^2 modes. The black line represents raw data that are fitted with the sum of individual functions (shown by blue lines) discussed in Appendix B. The red line represents individually fitted Raman modes.
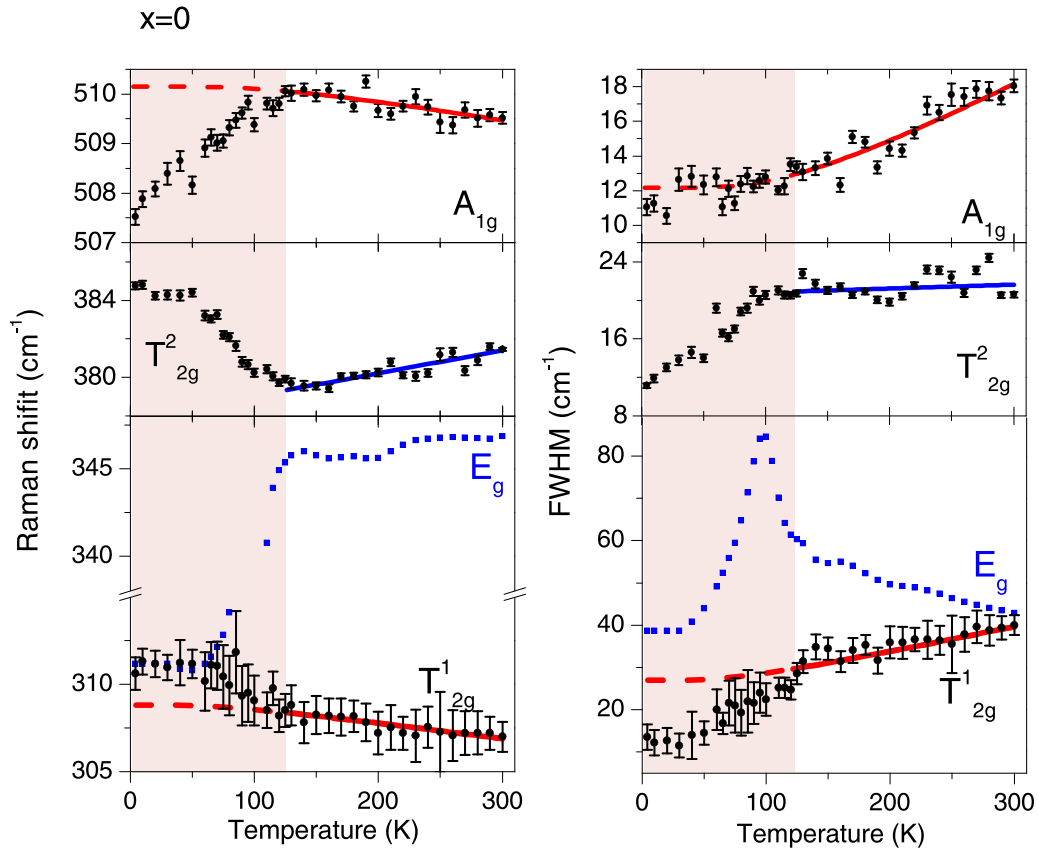
FIG. 4. Temperature dependence of frequency and linewidth of Raman modes T_{2g}^1, E_g, T_{2g}^2, and A_{1g} for $Eu_2Ir_2O_7$. The shaded region <122 K marks the magnetically ordered phase. Solid red lines are the fits of the cubic anharmonic model to the data above T_N, extrapolated to 0 K by the dashed lines. Blue lines above T_N are a guide to the eye. The solid blue squares represent E_g mode frequency and linewidth.

2. Raman anomalies for x = 0.02

For $x = 0.02$, the T_N decreases to 115 K. Figure 5(a) shows Raman spectra at different temperatures. Figure 5(b) shows Raman spectra at a few typical temperatures, highlighting the deconvolution using Lorentzian functions except for the E_g mode (Fano line shape). The modes $N1$ to $N5$ can be seen much below T_N. The parameters for the E_g mode $1/q$, ω_0, and Γ are taken to be the same as for the $x = 0$ sample [26], with its intensity as a fitting parameter. Figure 6 shows the temperature dependence of the frequency and linewidth of the four vibrational modes, which is like the case of undoped $Eu_2Ir_2O_7$. The additional features in the $x = 0.02$ system are (i) the linewidth of the A_{1g} mode is anomalous below T_N, i.e., it increases as T decreases, and most notably, (ii) the frequencies and linewidths show different temperature dependence $<\sim50$ K, which we identify as T^*, a crossover temperature in the AIAO phase [16].

3. Raman anomalies for x = 0.035

Figure 7(a) shows Raman spectra at different temperatures. Like for lower x values, Fig. 7(b) shows Raman spectra at a few typical temperatures, decomposed into T_{2g}^1, E_g, and T_{2g}^2. Here, we find that the fitting cannot resolve temperature dependence of the frequency, linewidth, and Fano parameter

$1/q$ of the E_g mode (Fig. 8). We focus only on the temperature dependence of the other three modes. Figure 9 shows the temperature dependence of the phonon frequency and linewidth for the four prominent modes, T_{2g}^1, T_{2g}^2, A_{1g}, and E_g modes. This brings out the following differences with respect to the temperature dependence of the corresponding modes for $x = 0$ and 0.02: The frequencies of T_{2g}^1, T_{2g}^2, and A_{1g} modes show change in their temperature dependence ~170 K. We note that the thermopower changes sign from being positive >170 K to negative below this temperature [16]. This can change the electron-phonon coupling, and hence, the non-monotonic temperature dependence of phonon frequencies above T_N is the combined effect of electron-phonon interaction and anharmonic interactions. We note that the linewidths of the modes do not show an anomalous temperature dependence above T_N, unlike the anomalous frequency dependence. As is known, the changes in frequency and linewidth arise from the real and imaginary parts of the self-energy of the phonon due to electron-phonon interaction. It is likely that the changes in the imaginary part of the self-energy (related to the linewidth) can be less than the real part. More theoretical work is needed to understand our results quantitatively. The solid lines are fit to the cubic anharmonic model between 300 and 170 K. Like $x = 0$ and 0.02, the A_{1g} mode frequency decreases and linewidth increases anomalously below T_N.
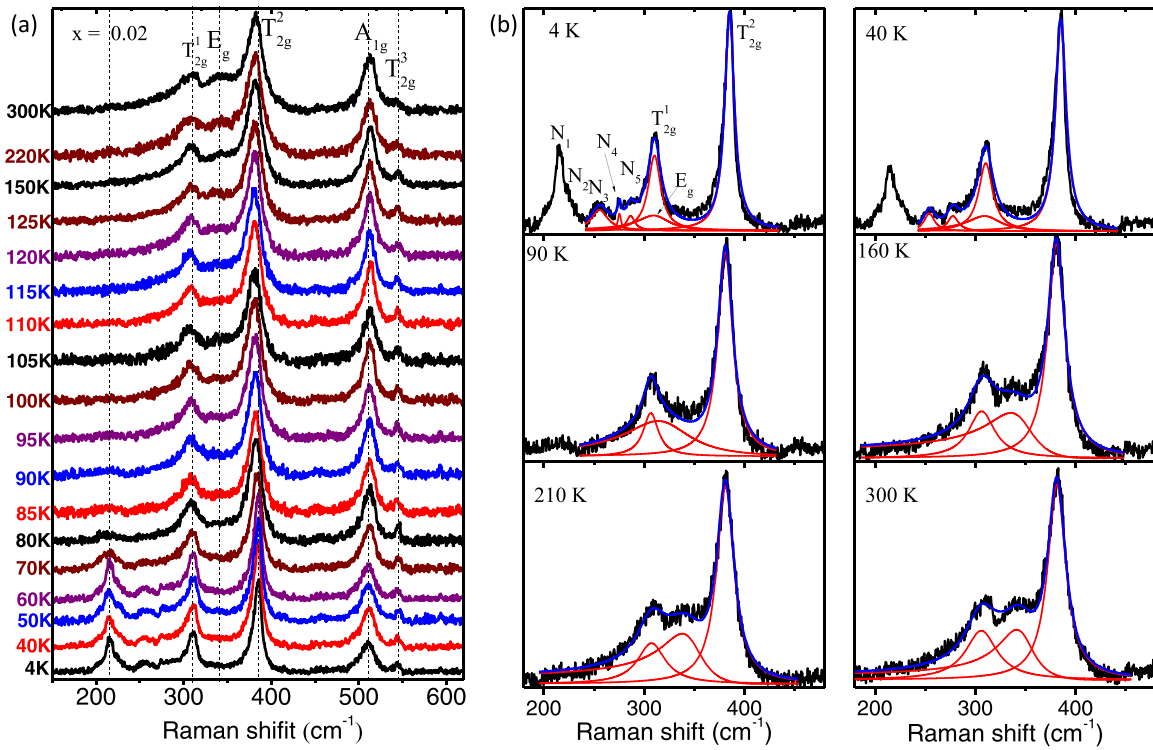
FIG. 5. (a) Raman spectra for $x = 0.02$ compound at several temperatures. (b) The representative plots for fitted data in the range of 180 to 480 cm^{-1}, covering T_{2g}^1, E_g, and T_{2g}^2 modes. The meaning of lines is the same as in Fig. 3.
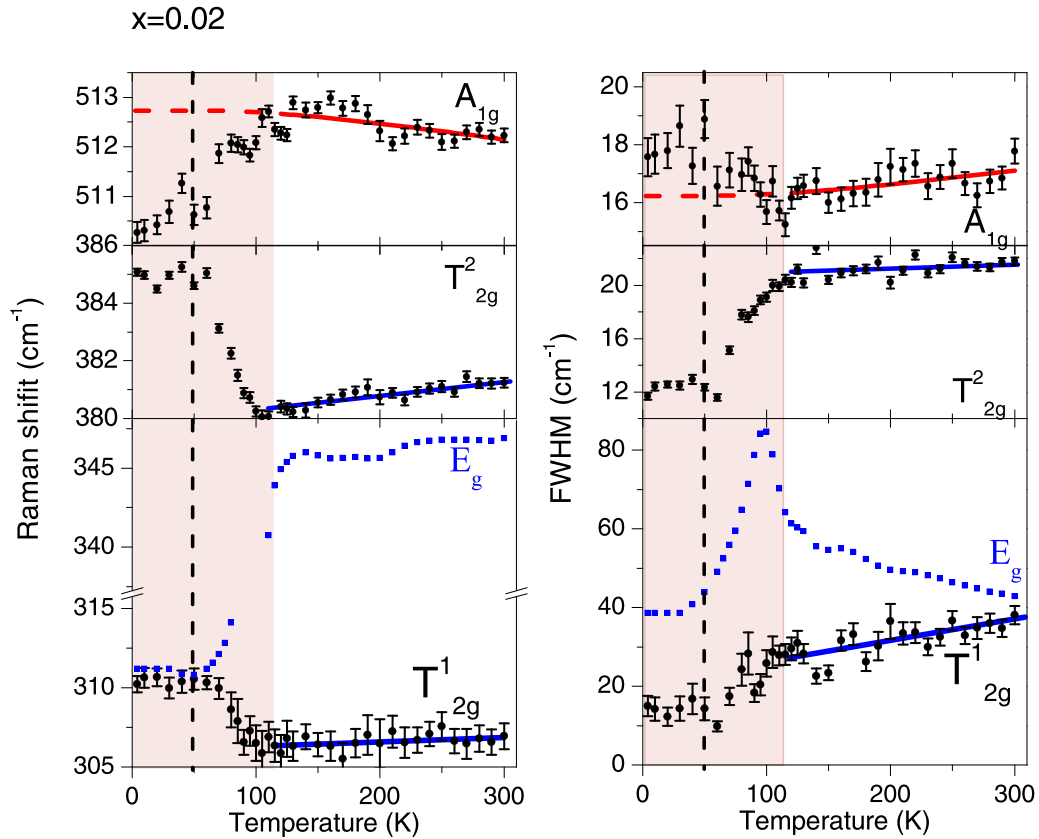
FIG. 6. Temperature dependence of frequency and linewidth of Raman modes T_{2g}^1, E_g, T_{2g}^2, and A_{1g} for $x = 0.02$. The shaded region <115 K marks the magnetically ordered phase. A vertical dashed line at 50 K marks T^*. The meaning of solid red and blue lines and solid blue symbols are the same as in Fig. 4.
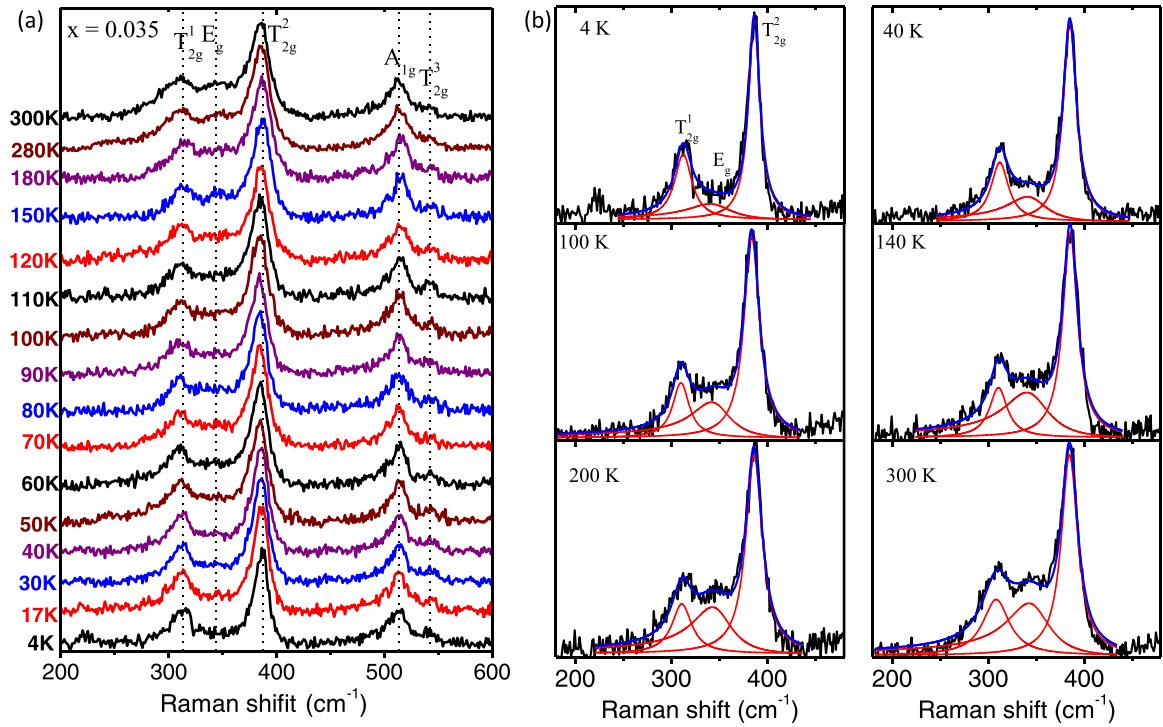
FIG. 7. (a) Raman spectra for $x = 0.035$ compound at several temperatures. (b) The representative plots of fitted data for selected temperatures in the range of 180 to 480 cm^{-1}, covering T_{2g}^1, E_g, and T_{2g}^2 modes. The meaning of lines is the same as in Fig. 3.

4. Raman spectra for x = 0.05

Figure 10(a) shows a stack plot of spectra recorded at different temperatures, and Fig. 10(b) shows spectra between 180 and 480 cm^{-1} resolved into three modes T_{2g}^1, E_g, and T_{2g}^2. Here, also, we cannot resolve the temperature dependence of the Fano parameters of the E_g mode, and hence, we discuss only the other three modes. Figure 11 shows the temperature dependence of frequency and linewidth of the T_{2g}^1, E_g, T_{2g}^2, and A_{1g} phonons. The frequencies of both low-frequency T_{2g} modes are significantly anomalous above $T_N (\sim 63$ K), shown by solid blue lines, due to the strong electron-phonon coupling in the metallic state. The A_{1g} mode again shows anomalous softening below T_N due to spin-phonon coupling.

5. Temperature dependence of Raman spectra for x = 0.1

Raman spectra at different temperatures are shown in Fig. 12(a). Like for Raman spectra for lower x values, Fig. 12(b) shows spectra at six typical temperatures resolved into T_{2g}^1, E_g, and T_{2g}^2 modes. Here, also, we do not focus on the E_g mode. For $x = 0$, the system remains metallic over the entire temperature range and shows Pauli paramagnetism [16]. The cubic anharmonic model in the entire temperature range can capture the trend of the A_{1g} mode, which hardens by ~ 2 cm^{-1} in frequency and becomes sharper at low temperatures (Fig. 13). The T_{2g} modes do not show much change with temperature.

IV. DISCUSSION

Before discussing the temperature dependence of various Raman modes, let us briefly recall the phase diagram of the $(Eu_{1-x}Bi_x)_2Ir_2O_7$ series previously reported in Ref. [16]. In this series, in the region $0 \leqslant x \leqslant 0.035$, the lattice parameter shows an anomalous contraction, and for $x \geqslant 0.1$, the lattice expands normally. The intermediate region $0.035 < x < 0.1$ is called the crossover region. For the convenience of the

FIG. 8. Asymmetric line shape parameter $1/q$ of E_g mode for various doping concentrations x.
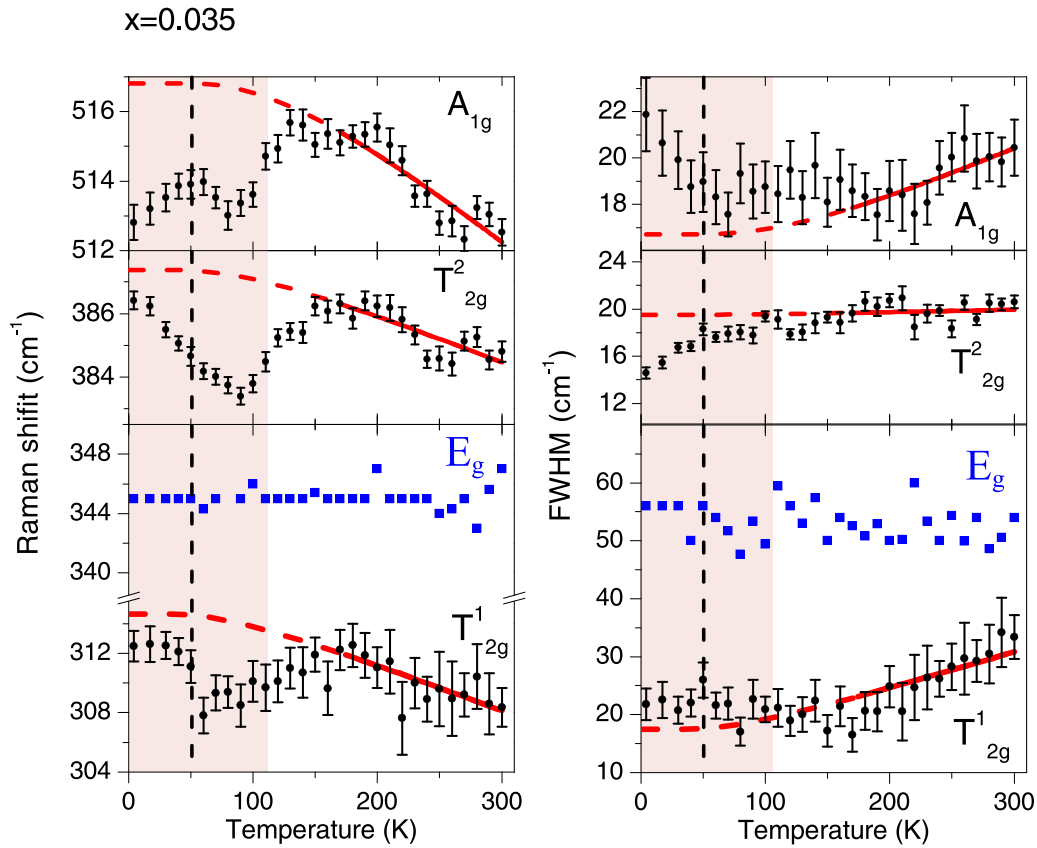
FIG. 9. Temperature dependence of frequency and linewidth of Raman modes T_{2g}^1, E_g, T_{2g}^2, and A_{1g} for $x = 0.035$. The shaded region <108 K marks the magnetically ordered phase. A vertical dotted line at 50 K marks T^*. The meaning of lines and symbols is the same as in Fig. 4.
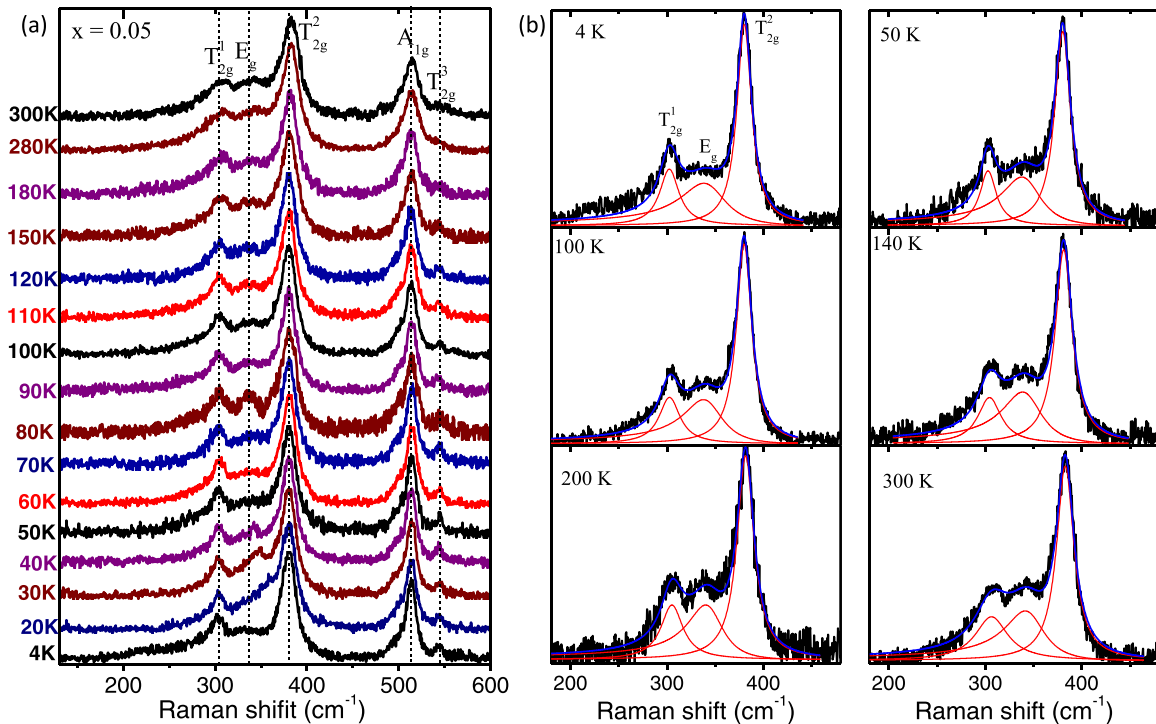
FIG. 10. (a) Raman spectra for $x = 0.05$ compound at several temperatures. (b) The representative plots for fitted data in the range of 180 to 480 cm^{-1}, covering T_{2g}^1, E_g, and T_{2g}^2 modes. The meaning of lines is the same as in Fig. 3.
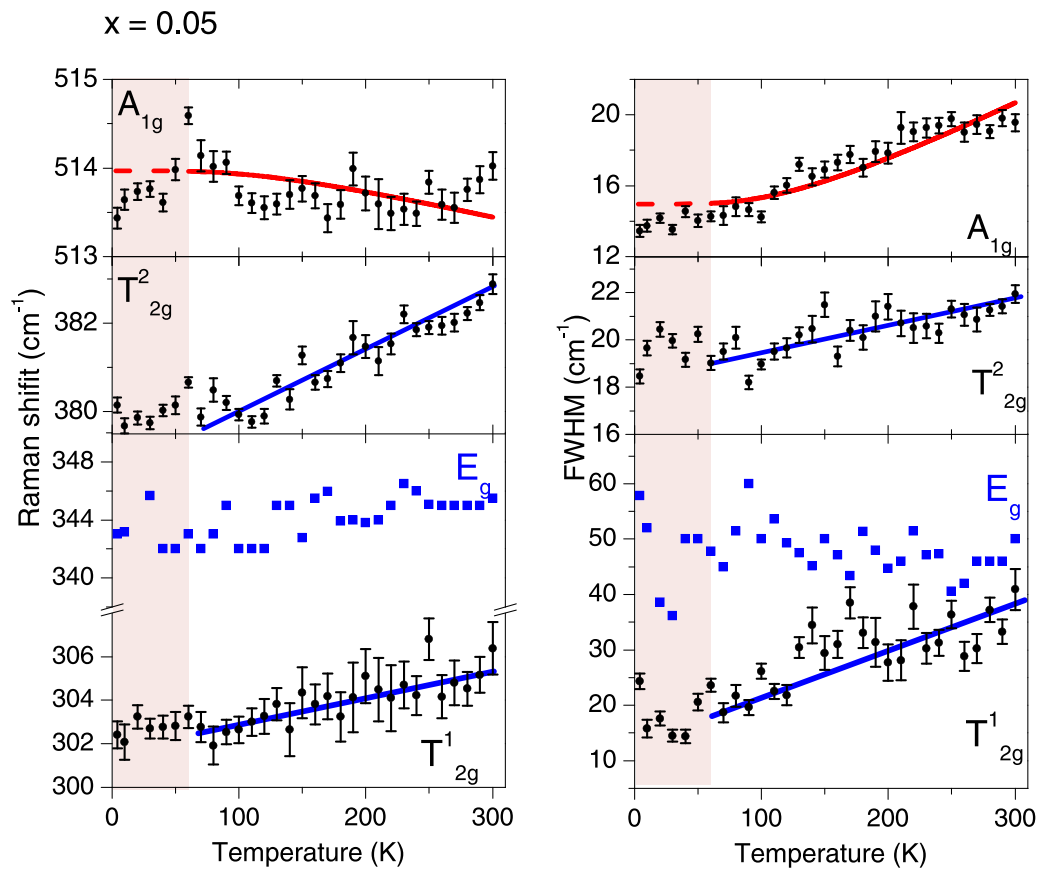
FIG. 11. Temperature dependence of frequency and linewidth of Raman modes T_{2g}^1, E_g, T_{2g}^2, and A_{1g} for $x = 0.05$. The shaded region <63 K marks the magnetically ordered phase. The meaning of lines and symbols is the same as in Fig. 4.
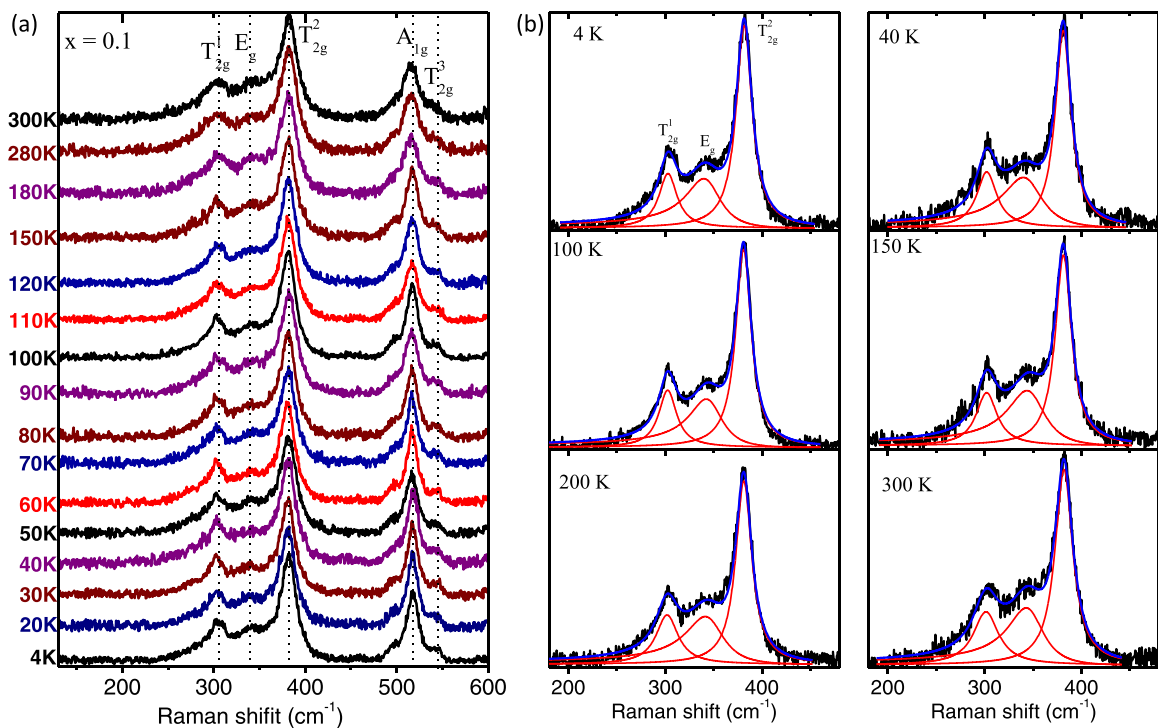
FIG. 12. (a) Raman spectra for $x = 0.1$ compound at several temperatures. (b) The representative plots for fitted data in the range of 180 to 480 cm^{-1}, covering T_{2g}^1, E_g, and T_{2g}^2 modes. The meaning of lines is the same as in Fig. 3.
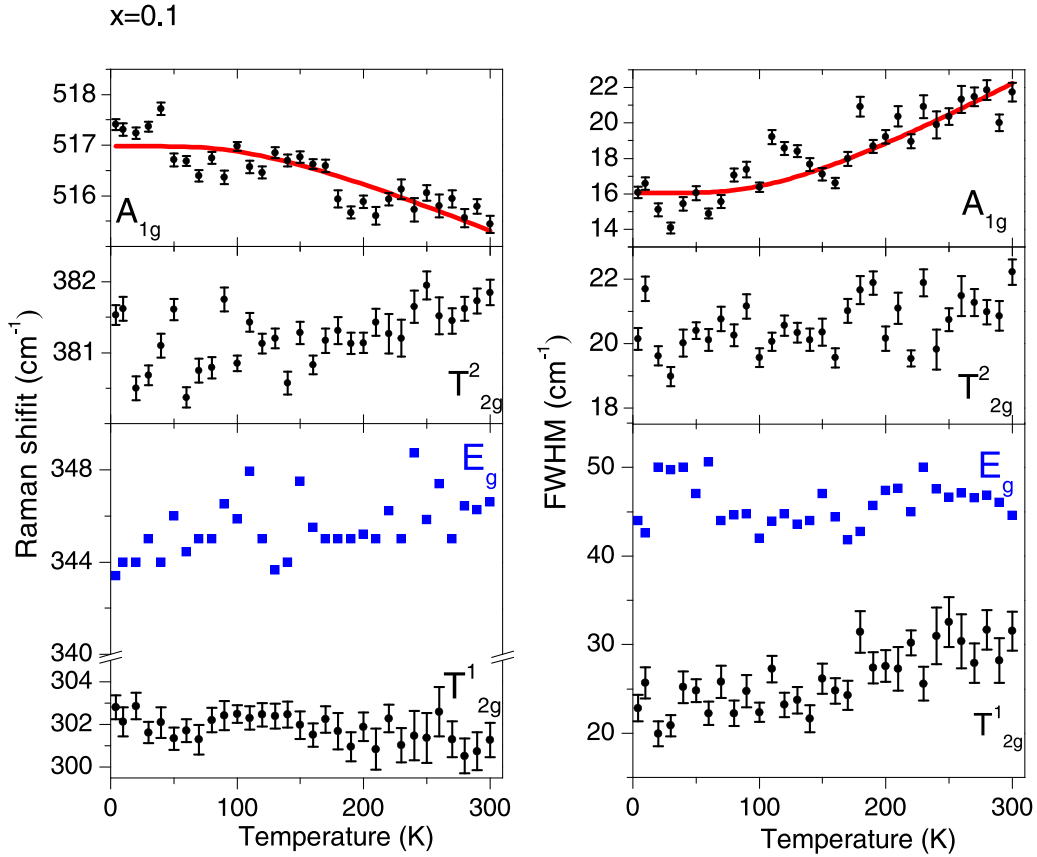
FIG. 13. Temperature dependence of frequency and linewidth of Raman modes T_{2g}^1, E_g, T_{2g}^2, and A_{1g} for $x = 0.1$. The meaning of lines and symbols is the same as in Fig. 4.

reader, in Fig. S2 in the Supplemental Material [29], the magnetic susceptibility and resistivity of the samples are replotted from Ref. [16]. As shown in Fig. S2 in the Supplemental Material [29], samples $x = 0$, 0.02, and 0.035 show a robust transition to a magnetically ordered phase below $T_N = 122$ K ($x = 0$), 115 K ($x = 0.02$), and 108 K ($x = 0.035$). For these samples, the resistivity also exhibits a sharp MIT at the same respective temperatures. For $x = 0.1$, on the other hand, no long-range ordering could be seen down to the lowest measured temperature, and it also shows a metallic behavior over the entire temperature range. The behavior of $x = 0.05$, which lies in the crossover region, is intermediate between these two limits: While the susceptibility of this sample shows a weak zero-field-cooled/field-cooled splitting $< \cong 60$ K, the resistivity shows a broad and shallow minimum centered around the same temperature.

We first focus on the softening of the A_{1g} mode below T_N in $x = 0$, 0.02, and 0.035. To qualitatively understand the frequency softening of the A_{1g} mode vis-à-vis the frequency hardening of the T_{2g} modes below T_N, we consider different contributions to spin-phonon coupling. The spin Hamiltonian can be written as $H = \sum_{i,j}[J_{IE}(S_i \cdot S_j) + D_{ij} \cdot (S_i \times S_j)]$ [27], where S_i and S_j are the $J_{\text{eff}} = \frac{1}{2}$ spins of Ir^{4+} at ith and jth positions in IrO_6 octahedra. Here, the first term is the Heisenberg IE interaction, and the second term is the DM interaction. The sign of D represents the chirality of spin texture. The effect of the anisotropic exchange interaction and

single-ion anisotropy are negligible for $J_{\text{eff}} = \frac{1}{2}$-related materials [27]. The spin-phonon coupling arises due to the dynamic modulation of the coefficients J_{IE} and D_{ij}. The effect of spin-phonon coupling due to the IE interaction has been observed in $3d$ multiferroic manganates [34], chromates [35–37], and $4d$ pyrochlore oxides [32]. The contribution of the IE interaction to the renormalization of a given phonon frequency arises from the modulation of J_{IE} by Ir-O vibrational amplitude (u) and Ir-O-Ir bond angle θ. This is given by $\Delta\omega \sim \lambda_{IE}(S_i \cdot S_j)$, where λ_{IE} is proportional to $\frac{\partial^2 J_{IE}(\theta)}{\partial \theta^2}$ and $\frac{\partial^2 J_{IE}(u)}{\partial u^2}$ [27,37]. The sign of λ_{IE} can be either positive or negative. In the case of the DM interaction, the spin-phonon coupling arises due to modulation of D_{ij} with respect to the Ir-O-Ir bond angle (θ). The phonon renormalization $\Delta\omega$ is proportional to $\sum_{i,j} \frac{\partial^2 D_{ij}(\theta)}{\partial \theta^2} \cdot (S_i \times S_j)$. The relative contributions of IE and DM due to modulation of respective exchange constants have been examined theoretically for $Y_2Ir_2O_7$ [27] and shown that, for $\theta \sim 130°$, the DM contributes an order of magnitude more to the phonon frequency renormalization than the IE.

In light of the above discussion, let us look at our results shown in Figs. 4, 6, and 9. The anomalous softening below T_N of the A_{1g} mode associated with the Ir-O-Ir bending vibrations is qualitatively like the observed softening of another bending vibrational E_g mode in the same system [26], and hence, both are expected to show similar

temperature dependence, though the magnitude of softening for the E_g mode ($\sim 10\%$) is much higher than that of the A_{1g} mode ($\sim 0.5\%$). This softening arises due to the spin-phonon coupling driven dominantly by the DM interaction with negative sign of $\frac{\partial^2 D_{ij}(\theta)}{\partial \theta^2}$. Similarly, the positive sign of λ_{IE} will result in hardening of the T_{2g} stretching modes below T_N for $x = 0$ and 0.02. The change of behavior below $T^* \sim 50$ K is possibly driven by the WSM ground state. As mentioned before, undoped and doped europium iridates show the WSM phase at low temperatures which will contribute to phonon renormalization [38,39]. In the gapless WSM state, the electron-hole excitations by the phonon with frequency $\omega(T)$ become possible, resulting in significant electron-phonon interaction. This contributes to additional softening of the phonon frequency and additional linewidth proportional to $H[\omega(0), T] = \{f[-\frac{\hbar\omega(0)}{2}] - f[\frac{\hbar\omega(0)}{2}]\}$, where f is the Fermi function. We note that spin-phonon coupling also contributes to the frequency shift and line broadening in addition to anharmonic interactions and electron-phonon coupling. Since the analytical form of the temperature dependence of spin-phonon coupling is not known, the data below T_N are not fitted with $H[\omega(0), T]$ (Fig. 6). At $x = 0.035$ also, the influence of the WSM state below T^* can be seen on phonon frequencies and linewidths, like the doped system with $x = 0.02$. In $x = 0.035$, the hardening of T_{2g} modes is seen only at low temperatures, and in $x = 0.05$, no hardening could be seen. This relates to the lowering of T_N or weakening of λ_{IE} due to increasing bandwidth, which is reflected in the increasing electrical conductivity (see Fig. S2 in the Supplemental Material [29]).

Next, we discuss the large decrease of the linewidths of the T_{2g}^1 and T_{2g}^2 modes below T_N. This anomalous decrease is most prominent in $x = 0$ and 0.02. This decrease can be attributed to the absence of electron-phonon coupling in the insulating AIAO phase, which also results in their corresponding frequency increase by a large amount. To sum up this part, our results point out the role of (a) the DM interaction in the anomalous temperature dependence of the A_{1g} mode, (b) the IE interaction for the stretching T_{2g} modes, which changes the bond length, and (c) the strong electron-phonon coupling in the metallic and WSM phases.

As shown in Fig. 2(b), a new mode marked $N1 \sim 211$ cm^{-1} (and some weak modes nearby) is seen below the AIAO transition temperature in $x = 0$, 0.02, and 0.035, i.e., the samples where a sharp magnetic transition to AIAO phase is observed. In $x = 0.05$, where the magnetic ground state has weakened considerably, the mode $N1$ is indistinguishable from the background; and finally, in $x = 0.1$, which does not show any magnetic ordering, no signs of $N1$ could be seen. Clearly, the presence of $N1$ can be associated with a robust magnetically ordered phase. By comparing inelastic x-ray scattering experiments, it has been suggested that the low-frequency mode $N1$ comes from single-magnon excitation [26,40] with a magnon excitation gap of ~ 28 meV, which is close to our observed Raman shift of ~ 26 meV. The temperature dependence of the $N1$ mode is discussed in Appendix C.

In addition to $N1$, we observe low-frequency Raman modes $N2$(~ 223 cm^{-1}), $N3$(~ 257 cm^{-1}), $N4$(~ 266 cm^{-1}), and $N5$(~ 277cm^{-1}) <50 K for undoped Eu$_2$Ir$_2$O$_7$ [Fig. 2(b)]. These modes can possibly be crystal field transitions of Eu^{3+}

that are coupled with phonons. The intensity of these modes decreases with doping, which can introduce structural distortions seen in various pyrochlores by lowering the cation site symmetry from D_{3d} to C_{3v} [41,42]. Structural distortions broaden the crystal field levels, which can be responsible for our not observing these at higher doping.

V. CONCLUSIONS

Our Raman studies have shown that the Ir-O-Ir bending mode A_{1g} and T_{2g}^1 and T_{2g}^2 modes, which have some contributions from the Ir-O stretching vibrations, are significantly influenced by strong spin-phonon coupling below T_N and strong electron-phonon coupling above T_N. Further, the emergence of the WSM phase at low temperatures ($<T^* \sim 50$ K) contributes to noticeable phonon renormalization. These results add to the exploration of properties of pyrochlore iridates arising from spin-phonon and electron-phonon interactions. We hope that our detailed experimental results will motivate further theoretical calculations to understand phonon anomalies quantitatively in the AIAO phase as well as above T_N.

APPENDIX A: DETAILS OF RAMAN AND X-RAY CHARACTERIZATION AT AMBIENT CONDITION

Figure 14(a) shows the Raman spectra for $x = 0$, 0.02, 0.035, 0.05, and 0.1 in the range 190-850 cm^{-1} at ambient condition. The Raman spectra were fitted with the sum of Lorentzians for all the modes except the E_g mode, which was fitted with a Fano line shape profile by nonlinear least square fitting using ORIGIN software. The extracted frequencies for various Raman modes are plotted with doping concentration x in Fig. 14(b), where the E_g mode Fano parameter $1/q$ is taken from Ref. [26] for $x = 0$ and 0.02, and for other doping, $1/q = -0.16$ is seen to give good fit to the data. We also plot in Fig. 14(c) the doping dependence of the Ir-O bond length and the Ir-O-Ir angle (obtained from the Rietveld analysis of x-ray diffraction data) at ambient temperature to see the correlation between the mode frequencies and structural parameters. The two bending modes E_g and A_{1g} are influenced differently by doping. There is no simple correlation which suggests that the mode frequencies are also renormalized significantly due to electron-phonon coupling in the metallic state.
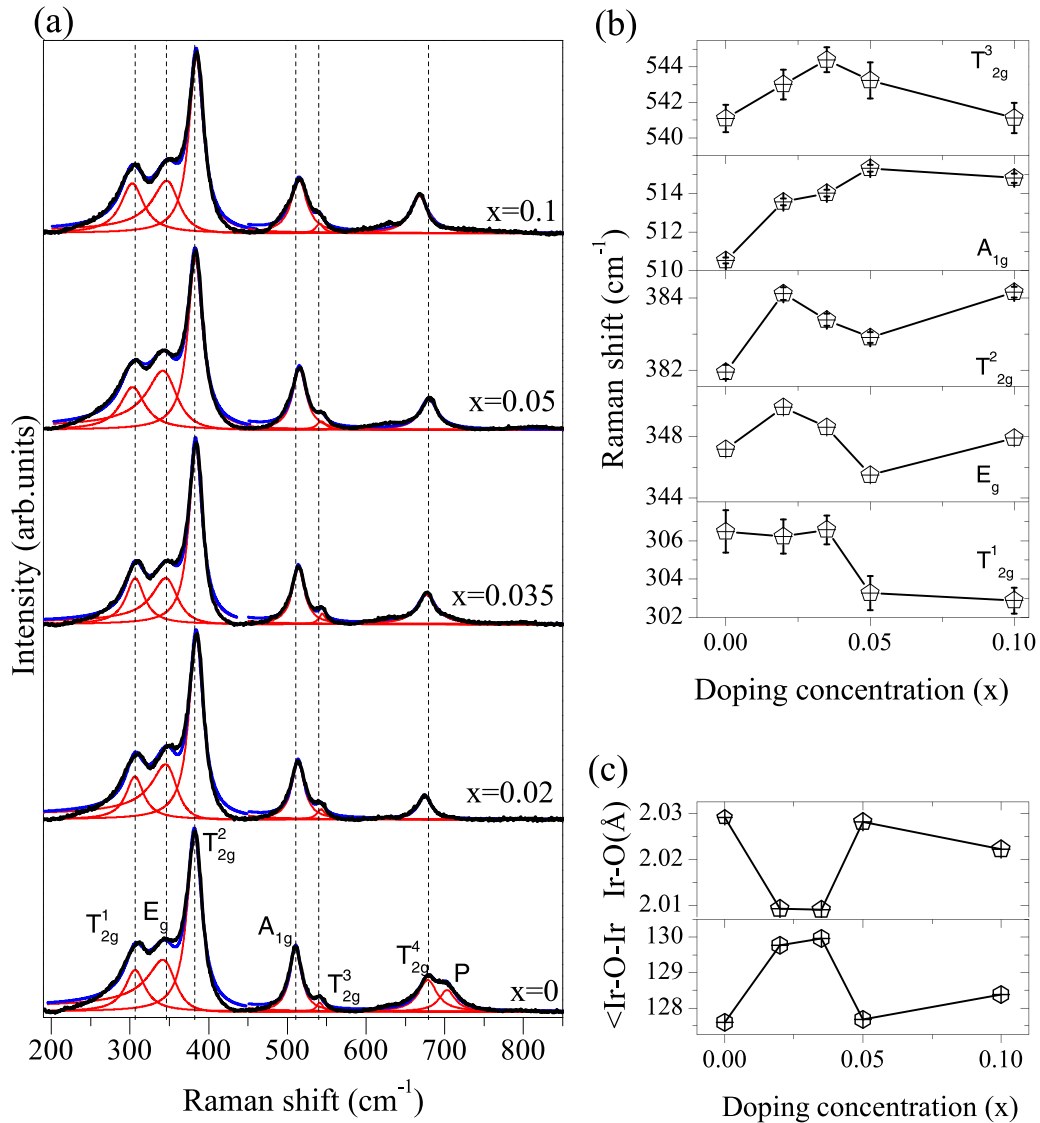
FIG. 14. (a) Raman spectra of $(Eu_{1-x}Bi_x)_2Ir_2O_7$ at room temperature. The black line represents raw data that are fitted with a sum of individual functions (shown by blue lines) discussed in Appendix A. The red line represents individually fitted Raman modes. (b) Raman frequencies as a function of doping concentration x. (c) Evolution of Ir-O bond length and Ir-O-Ir bond angle vs x. Solid lines in (b) and (c) are a guide to the eye.

APPENDIX B: DETAILS OF FANO-LORENTZ MODEL USED FOR FITTING

We have analyzed the data in the range of 180 to 480 cm^{-1}, covering T_{2g}^1, E_g, and T_{2g}^2 modes by taking the Fano line shape for the E_g mode and Lorentzian line shape for the T_{2g}^1 and T_{2g}^2 modes. Panels (a) of Figs. 3, 5, 7, 10, and 12 show the evolution of Raman spectra with temperature and panels (b) of Figs. 3, 5, 7, 10, and 12 show fitted Raman spectra at a few typical temperatures for different x values. As the E_g mode in our unpolarized Raman spectra overlaps with T_{2g}^1 and T_{2g}^2, we were guided by Ref. [26] in fixing the parameters $1/q$ (Fig. 8), frequency and linewidth (Fig. 4) values for $x = 0$, and keeping the intensity of the E_g mode as the fitting parameter in the temperature range 30–300 K. Below 30 K, $1/q$ does not change. For $x = 0.02$, we find that the best fit could be obtained by taking the parameter of the E_g mode the same

as for the $x = 0$ sample. However, for $x = 0.035$, 0.05, and 0.1, the $1/q$ value was taken to be ~ -0.16 in the entire temperature range to fit the data (Fig. 8). All the other modes were taken to be Lorentzian, and the parameters were obtained by nonlinear least square fit. The error bars on the value of frequencies and linewidth are obtained from the nonlinear least square fitting of the data with the desired line shape (Lorentzian for all modes except the Fano function for the E_g mode).

APPENDIX C: TEMPERATURE DEPENDENCE OF MAGNON MODE (N1)

The temperature dependence of the $N1$ mode frequency and its intensity relative to the T_{2g}^2 phonon are plotted in Figs. 15(a) and 15(b) for $x = 0$ and 0.02, respectively. A slight hardening of $N1$ with x can be attributed to the higher
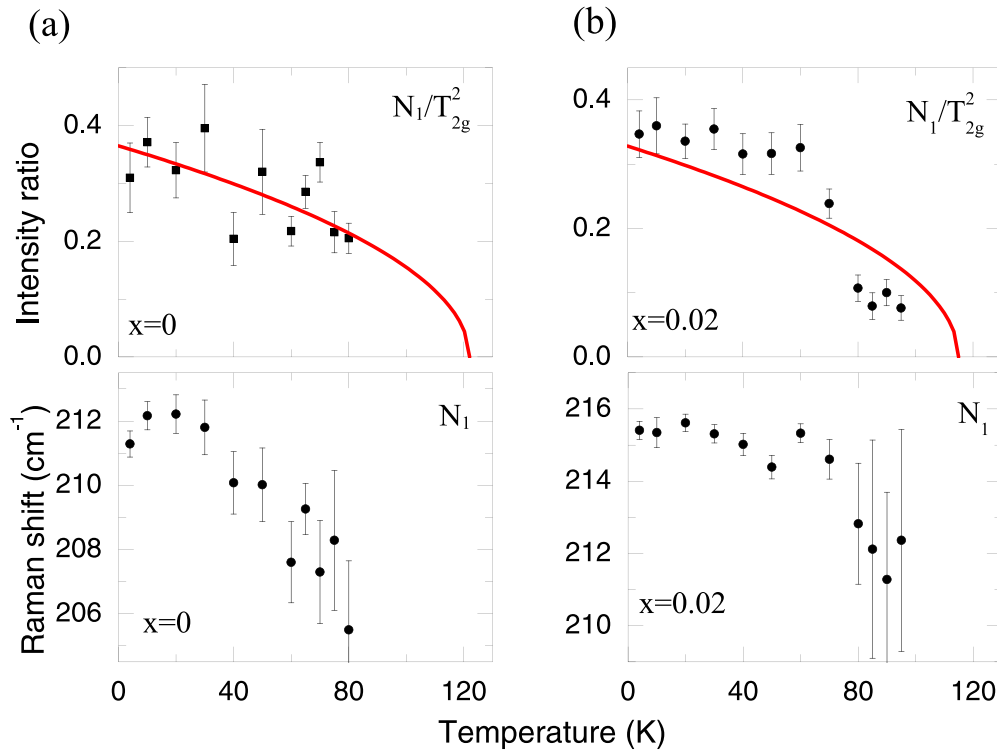
FIG. 15. Temperature dependence of frequency (bottom panels) and relative intensities (top panels) of the one magnon Raman mode $N1$ for (a) $x = 0$ and (b) $x = 0.02$. The red solid lines are fit to the experimental data as discussed in the text.

spin-exchange constant expected due to lattice contraction. Taking the intensity of the $N1$ mode as an order parameter, the red line is a fit to $\sim (T_N - T)^{1/2}$, as expected in the mean field theory.

[1] D. Pesin and L. Balents, Mott physics and band topology in materials with strong spin-orbit interaction, Nat. Phys. **6**, 376 (2010).

[2] W. Witczak-Krempa, G. Chen, Y. B. Kim, and L. Balents, Correlated quantum phenomena in the strong spin-orbit regime, Annu. Rev. Condens. Matter Phys. **5**, 57 (2014).

[3] X. Wan, A. M. Turner, A. Vishwanath, and S. Y. Savrasov, Topological semimetal and Fermi-arc surface states in the electronic structure of pyrochlore iridates, Phys. Rev. B **83**, 205101 (2011).

[4] H. Shinaoka, Y. Motome, T. Miyake, S. Ishibashi, and P. Werner, First-principles studies of spin-orbital physics in pyrochlore oxides, J. Phys. Condens. Matter **31**, 323001 (2019).

[5] K. Matsuhira, M. Wakeshima, Y. Hinatsu, and S. Takagi, Metal-insulator transitions in pyrochlore oxides $Ln_2Ir_2O_7$, J. Phys. Soc. Japan **80**, 094701 (2011).

[6] D. Yanagishima and Y. Maeno, Metal-nonmetal changeover in pyrochlore iridates, J. Phys. Soc. Japan **70**, 2880 (2001).

[7] T. F. Qi, O. B. Korneta, X. Wan, L. E. DeLong, P. Schlottmann, and G. Cao, Strong magnetic instability in correlated metallic $Bi_2Ir_2O_7$, J. Phys. Condens. Matter **24**, 345601 (2012).

[8] K. Matsuhira, M. Wakeshima, R. Nakanishi, T. Yamada, A. Nakamura, W. Kawano, S. Takagi, and Y. Hinatsu, Metal-insulator transition in pyrochlore iridates $Ln_2Ir_2O_7$ (Ln = Nd, Sm, and Eu), J. Phys. Soc. Japan **76**, 43706 (2007).

[9] Y. Wang, T. F. Rosenbaum, D. Prabhakaran, A. T. Boothroyd, and Y. Feng, Approaching the quantum critical point in a highly correlated all-in–all-out antiferromagnet, Phys. Rev. B **101**, 220404 (2020).

[10] H. Takatsu, K. Watanabe, K. Goto, and H. Kadowaki, Comparative study of low-temperature x-ray diffraction experiments on $R_2Ir_2O_7$ (R = Nd, Eu, and Pr), Phys. Rev. B **90**, 235110 (2014).

[11] W. Witczak-Krempa and Y. B. Kim, Topological and magnetic phases of interacting electrons in the pyrochlore iridates, Phys. Rev. B **85**, 045124 (2012).

[12] A. B. Sushkov, J. B. Hofmann, G. S. Jenkins, J. Ishikawa, S. Nakatsuji, S. Das Sarma, and H. D. Drew, Optical evidence for a Weyl semimetal state in pyrochlore $Eu_2Ir_2O_7$, Phys. Rev. B **92**, 241108(R) (2015).

[13] F. F. Tafti, J. J. Ishikawa, A. McCollam, S. Nakatsuji, and S. R. Julian, Pressure-tuned insulator to metal transition in $Eu_2Ir_2O_7$, Phys. Rev. B **85**, 205104 (2012).

[14] M. Nakayama, T. Kondo, Z. Tian, J. J. Ishikawa, M. Halim, C. Bareille, W. Malaeb, K. Kuroda, T. Tomita, S. Ideta, K. Tanaka, M. Matsunami, S. Kimura, N. Inami, K. Ono, H. Kumigashira, L. Balents, S. Nakatsuji, and S. Shin, Slater to Mott Crossover in the Metal to Insulator Transition of $Nd_2Ir_2O_7$, Phys. Rev. Lett. **117**, 056403 (2016).

[15] K. Ueda, J. Fujioka, and Y. Tokura, Variation of optical conductivity spectra in the course of bandwidth-controlled

metal-insulator transitions in pyrochlore iridates, Phys. Rev. B **93**, 245120 (2016).

[16] P. Telang, K. Mishra, G. Prando, A. K. Sood, and S. Singh, Anomalous lattice contraction and emergent electronic phases in Bi-doped $Eu_2Ir_2O_7$, Phys. Rev. B **99**, 201112 (2019).

[17] K. Ueda, J. Fujioka, Y. Takahashi, T. Suzuki, S. Ishiwata, Y. Taguchi, and Y. Tokura, Variation of Charge Dynamics in the Course of Metal-Insulator Transition for Pyrochlore-Type $Nd_2Ir_2O_7$, Phys. Rev. Lett. **109**, 136402 (2012).

[18] H. Kumar, V. G. Sathe, and A. K. Pramanik, Spin-phonon coupling in hole-doped pyrochlore iridates $Y_2Ir_2O_7$, J. Magn. Magn. Mater. **478**, 148 (2019).

[19] H. Kumar, R. S. Dhaka, and A. K. Pramanik, Evolution of structure, magnetism, and electronic transport in the doped pyrochlore iridate $Y_2Ir_{2-x}Ru_xO_7$, Phys. Rev. B **95**, 054415 (2017).

[20] B. J. Yang and Y. B. Kim, Topological insulators and metal-insulator transition in the pyrochlore iridates, Phys. Rev. B **82**, 085111 (2010).

[21] X. Zhang, Y. Zhang, S. Okamoto, and D. Xiao, Thermal Hall Effect Induced by Magnon-Phonon Interactions, Phys. Rev. Lett. **123**, 167202 (2019).

[22] X. Moya and N. D. Mathur, Turn your phonon, Nat. Mater. **16**, 784 (2017).

[23] J. T. Zhang, C. Ji, J. L. Wang, W. S. Xia, X. M. Lu, and J. S. Zhu, Stabilization of E-type magnetic order caused by epitaxial strain in perovskite manganites, Phys. Rev. B **97**, 085124 (2018).

[24] R. Ramesh and N. A. Spaldin, Multiferroics: Progress and prospects in thin films, Nat. Mater. **6**, 21 (2007).

[25] C. Calero, E. M. Chudnovsky, and D. A. Garanin, Field Dependence of the Electron Spin Relaxation in Quantum Dots, Phys. Rev. Lett. **95**, 166603 (2005).

[26] K. Ueda, R. Kaneko, A. Subedi, M. Minola, B. J. Kim, J. Fujioka, Y. Tokura, and B. Keimer, Phonon anomalies in pyrochlore iridates studied by Raman spectroscopy, Phys. Rev. B **100**, 115157 (2019).

[27] J. Son, B. C. Park, C. H. Kim, H. Cho, S. Y. Kim, L. J. Sandilands, C. Sohn, J. G. Park, S. J. Moon, and T. W. Noh, Unconventional spin-phonon coupling via the Dzyaloshinskii-Moriya interaction, npj Quantum Mater. **4**, 17 (2019).

[28] A. C. Dippel, H. P. Liermann, J. T. Delitz, P. Walter, H. Schulte-Schrepping, O. H. Seeck, and H. Franz, Beamline P02.1 at PETRA III for high-resolution and high-energy powder diffraction, J. Synchrotron Radiat. **22**, 675 (2015).

[29] See Supplemental Material at http://link.aps.org/supplemental/10.1103/PhysRevB.105.075145 for x-ray diffraction data with Rietveld refinement for $x = 0$ and 0.02, resistivity and magnetic susceptibility plots for $x = 0$, 0.02, 0.035, 0.05, and 0.1 of $(Eu_{1-x}Bi_x)_2Ir_2O_7$.

[30] S. Saha, D. V. S. Muthu, S. Singh, B. Dkhil, R. Suryanarayanan, G. Dhalenne, H. K. Poswal, S. Karmakar, S. M. Sharma, A. Revcolevschi, and A. K. Sood, Low-temperature and high-pressure Raman and x-ray studies of pyrochlore $Tb_2Ti_2O_7$, Phys. Rev. B **79**, 134112 (2009).

[31] M. T. Vandenborre, E. Husson, J. P. Chatry, and D. Michel, Rare-earth titanates and stannates of pyrochlore structure; vibrational spectra and force fields, J. Raman Spectrosc. **14**, 63 (1983).

[32] J. S. Bae, I.-S. Yang, J. S. Lee, T. W. Noh, T. Takeda, and R. Kanno, Raman scattering study of the geometrically frustrated pyrochlore $Y_2Ru_2O_7$, Vib. Spectrosc. **42**, 284 (2006).

[33] P. G. Klemens, Anharmonic decay of optical phonons, Phys. Rev. **148**, 845 (1966).

[34] J. Laverdière, S. Jandl, A. A. Mukhin, V. Y. Ivanov, V. G. Ivanov, and M. N. Iliev, Spin-phonon coupling in orthorhombic $RMnO_3$ (R = Pr, Nd, Sm, Eu, Gd, Tb, Dy, Ho, Y): A Raman study, Phys. Rev. B **73**, 214301 (2006).

[35] R. Valdés Aguilar, A. B. Sushkov, Y. J. Choi, S. W. Cheong, and H. D. Drew, Spin-phonon coupling in frustrated magnet $CdCr_2O_4$, Phys. Rev. B **77**, 092412 (2008).

[36] C. Kant, J. Deisenhofer, T. Rudolf, F. Mayr, F. Schrettle, A. Loidl, V. Gnezdilov, D. Wulferding, P. Lemmens, and V. Tsurkan, Optical phonons, spin correlations, and spin-phonon coupling in the frustrated pyrochlore magnets $CdCr_2O_4$ and $ZnCr_2O_4$, Phys. Rev. B **80**, 214417 (2009).

[37] B. S. Araújo, A. M. Arévalo-López, C. C. Santos, J. P. Attfield, C. W. A. Paschoal, and A. P. Ayala, Spin-phonon coupling in monoclinic $BiCrO_3$, J. Appl. Phys. **127**, 114102 (2020).

[38] M. Kuiri, S. Das, D. V. S. Muthu, A. Das, and A. K. Sood, Thickness dependent transition from the 1T′ to Weyl semimetal phase in ultrathin $MoTe_2$: Electrical transport, noise and Raman studies, Nanoscale **12**, 8371 (2020).

[39] B. Xu, Y. M. Dai, L. X. Zhao, K. Wang, R. Yang, W. Zhang, J. Y. Liu, H. Xiao, G. F. Chen, S. A. Trugman, J.-X. Zhu, A. J. Taylor, D. A. Yarotski, R. P. Prasankumar, and X. G. Qiu, Temperature-tunable Fano resonance induced by strong coupling between Weyl fermions and phonons in TaAs, Nat. Commun. **8**, 14933 (2017).

[40] S. H. Chun, B. Yuan, D. Casa, J. Kim, C. Y. Kim, Z. Tian, Y. Qiu, S. Nakatsuji, and Y. J. Kim, Magnetic Excitations across the Metal-Insulator Transition in the Pyrochlore Iridate $Eu_2Ir_2O_7$, Phys. Rev. Lett. **120**, 177203 (2018).

[41] S. Muñoz Pérez, R. Cobas, J. M. Cadogan, J. Albino Aguiar, S. V. Streltsov, and X. Obradors, Ruthenium-europium configuration in the $Eu_2Ru_2O_7$ pyrochlore, J. Appl. Phys. **117**, 17C702 (2015).

[42] K. A. Ross, J. M. Brown, R. J. Cava, J. W. Krizan, S. E. Nagler, J. A. Rodriguez-Rivera, and M. B. Stone, Single-ion properties of the $S_{eff} = \frac{1}{2}$ XY antiferromagnetic pyrochlores $NaA'Co_2F_7(A' = Ca^{2+}, Sr^{2+})$, Phys. Rev. B **95**, 144414 (2017).